

Planetary geophysics

Physics of the Earth as a Planet, Lecture 11

	Venus	Earth	Mars
Mass	4.87×10^{24} kg	5.97×10^{24} kg	0.642×10^{24} kg
Radius	6052 km	6373 km	3396 km
1° latitude	106 km	111 km	59 km
Orbital period	224.7 Earth days	365.2 Earth days	687.0 Earth days
Mean distance from Sun	1.082×10^8 km	1.496×10^8 km	2.279×10^8 km
Rotation rate	243 Earth days/rev	1 Earth day/rev	1.03 Earth day/rev
Density	5.2 Mg/m^3	5.5 Mg/m^3	3.9 Mg/m^3
Surface gravity	8.87 m s^{-2}	9.81 m s^{-2}	3.70 m s^{-2}
Surface pressure	9 MPa	0.1 MPa	0.001 MPa
Surface temperature	430°C	10°C	-65°C
Magnetic moment	$< 3 \times 10^{11} \text{ T m}^3$	$7.5 \times 10^{15} \text{ T m}^3$	$< 2 \times 10^{11} \text{ T m}^3$

Venus

Venus is always covered by clouds, of sulphuric acid droplets, and so its surface cannot be photographed. Therefore the only way of mapping its surface is by radar. The major problem with radar is power: the radiated and scattered energies both decrease as $1/r^2$, so the returned power decreases as $1/r^4$. Any satellite must be above the atmosphere, and therefore at a height of 200 km. It is important that the angle between the incident beam and the horizontal should be as small as possible, which requires the radar to illuminate the surface as far as possible from its ground track. Since the power for the radar must come from solar cells, the design of this part of the spacecraft dominated its construction. The radar was a synthetic aperture radar (a SAR), in which the resolution along track comes from the Doppler shift of the echo, that across track from the time of flight. It radiates only 200 Watts.

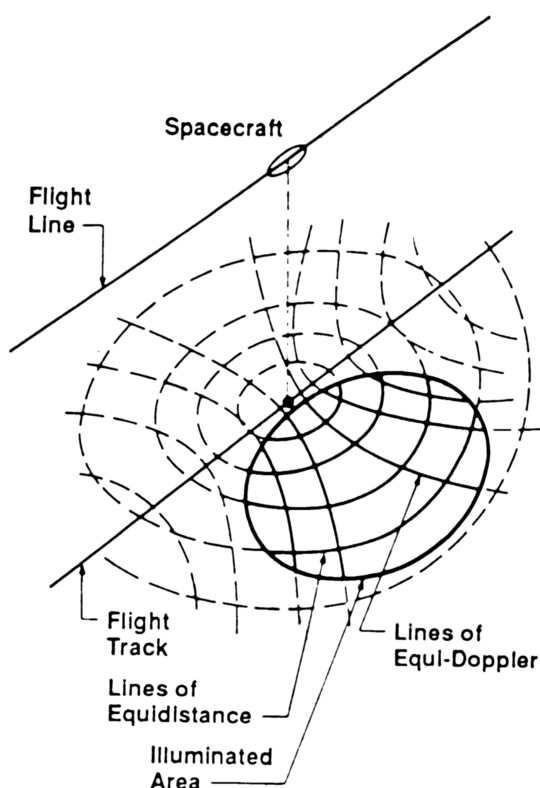


Figure 1: Constant time-delay and Doppler contour lines that form the radar-imaging coordinate system. Image resolution elements are defined by intersections of Doppler resolution elements and time-delay resolution elements. The brightness in each image resolution element is proportional to the back scattered energy.

The Magellan SAR operated at a wavelength of 125 mm, and the brightness variations in the images result from variations in surface roughness on this scale. SARs produce several artifacts. If they image a target that has a velocity component along the radar beam the location of the target in the image is in error. So the cars on the Golden Gates bridge in San Francisco appear to be driving over the water.

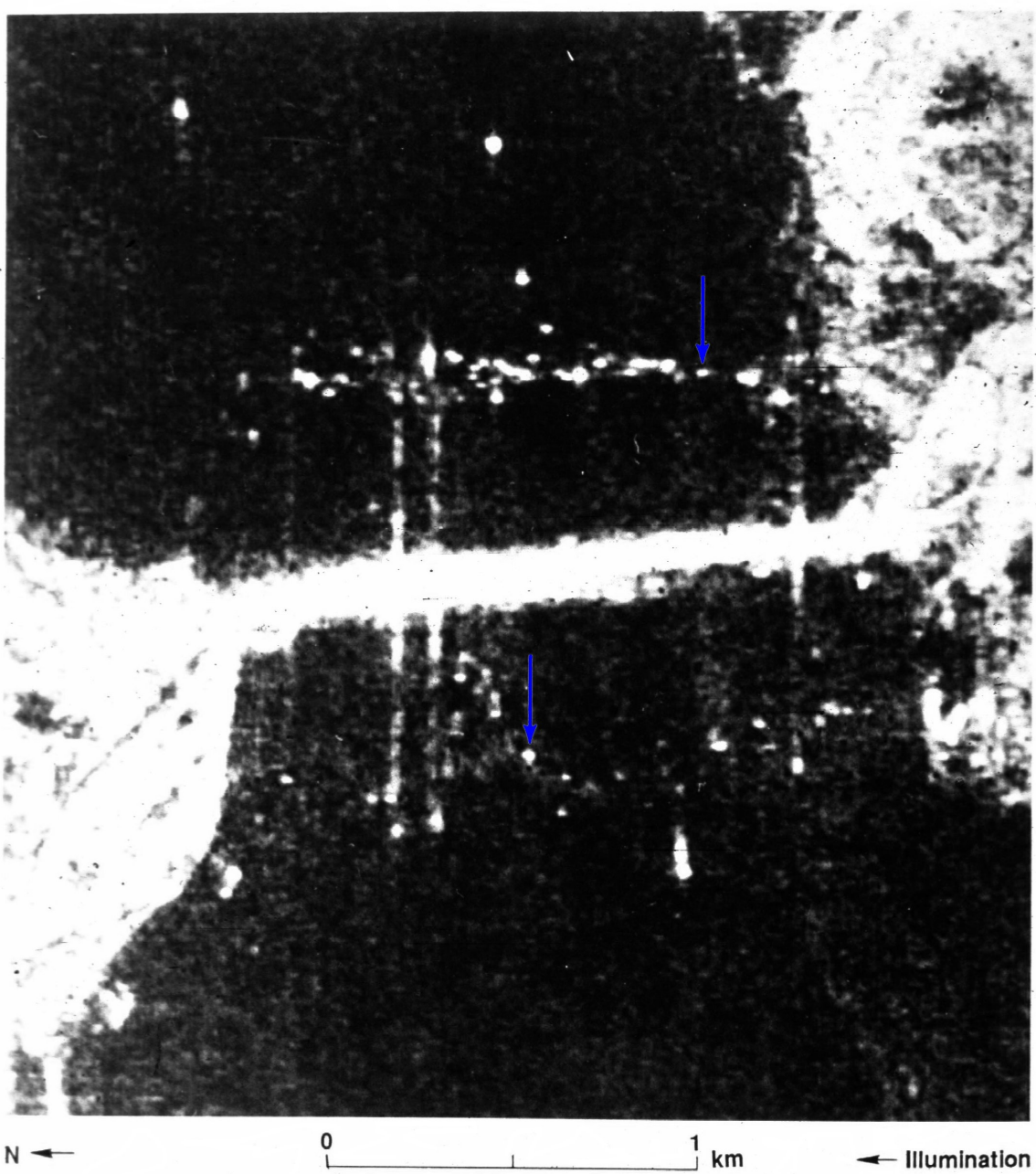


Figure 2: JPL aircraft SAR image of Golden Gate Bridge, San Francisco. Traffic going across the bridge is mispositioned because of its movement with respect to the bridge.

A more important problem on Venus is that steep slopes return an echo from the top of the slope first and so the top of the slope appears to be closer at its base (Figure 3). Figure 4 shows an extreme case of this problem, where the image of the top of a U shaped valley in Alaska maps onto the glacier on the valley floor.

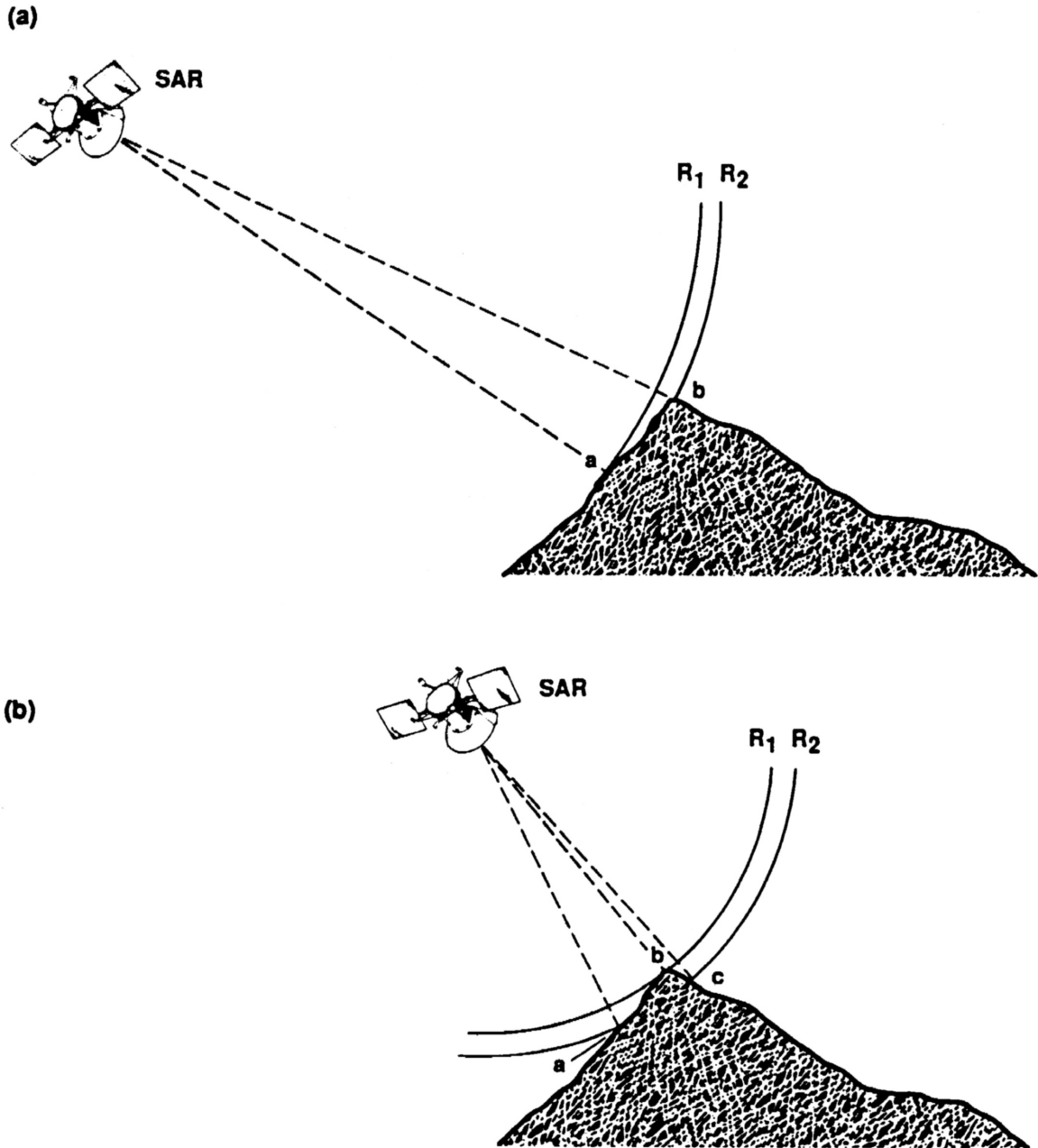


Figure 3: A diagram showing how overlay can occur. In (a) the reflection from the base of the mountain will arrive before the reflection from the peak of the mountain, and features will be properly placed in the image. However, in (b), where there is a smaller angle of incidence, the reflection from the peak of the mountain will arrive before the reflection from the base, causing overlay in the image (see Figure 4).

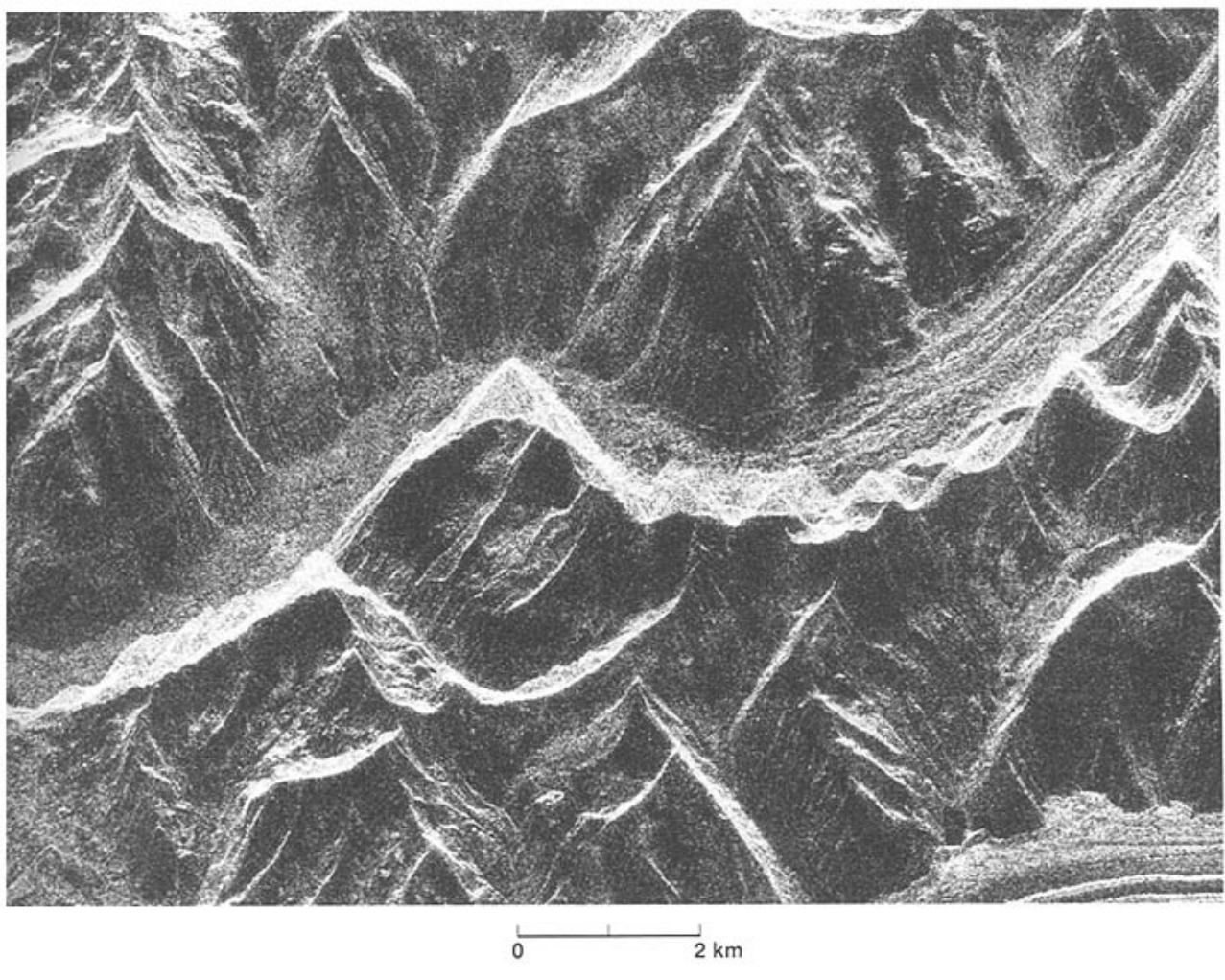


Figure 4: Seasat image of a portion of the Alaska Range showing overlay of a ridge and peak adjacent to a glacier filled valley.

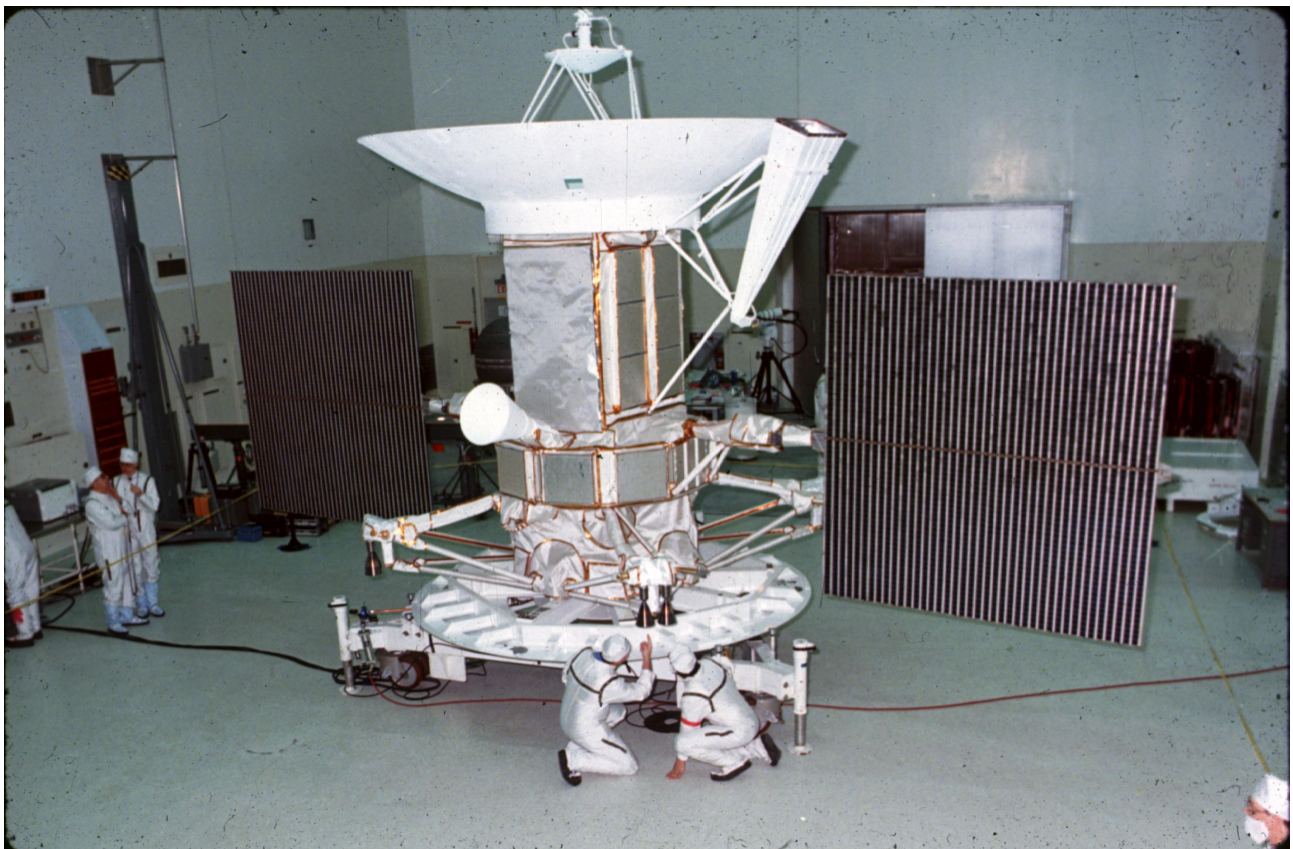


Figure 5: NASA's Magellan spacecraft.

The spacecraft operated by imaging the surface of Venus and recording the results on a tape recorder. The whole spacecraft then rotated to point at the Earth, and played back the data. Each orbit took about 3 hours, and it carried out these manoeuvres every orbit for two years. We now have better maps of Venus, and better knowledge of its topography, than we do of Earth. But we don't know much else about the planet, so understanding its tectonic and thermal history is still quite difficult. The spectacular images show many surface features on Venus whose origin is easily understood. There are a large number of impact craters, some of which are very big (Figure 6).

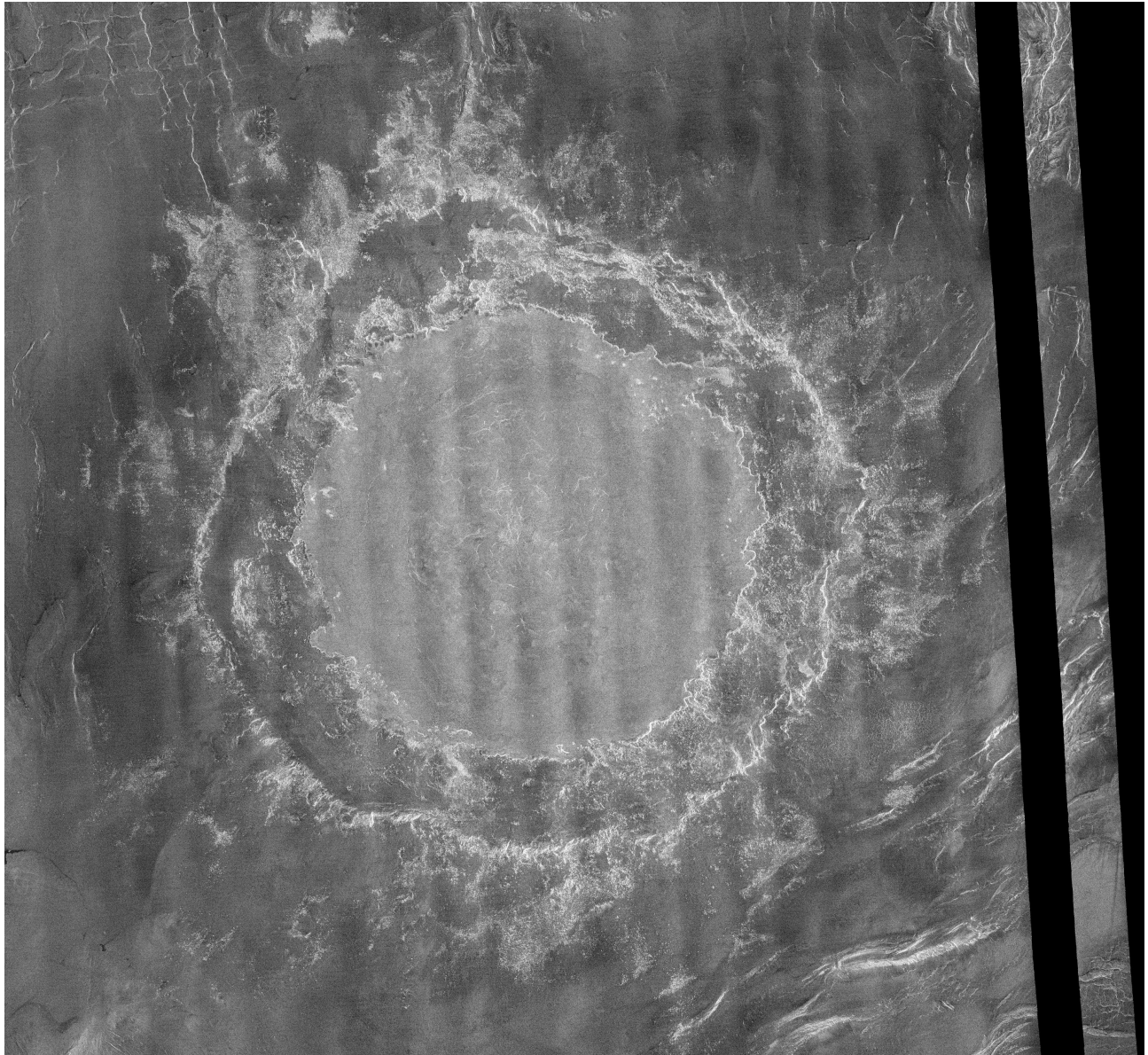


Figure 6: This Magellan image mosaic shows the largest (275 km) impact crater known to exist on Venus. The crater is located north of Aphrodite Terra and east of Eistla Regio at latitude 12.5°N and longitude 57.4°E . This crater is named Mead, and is classified as a multi-ring crater with its innermost, concentric scarp being interpreted as the rim of the original crater cavity. The flat, somewhat brighter inner floor of Mead is interpreted to result from considerable infilling of the original crater cavity by impact melt and/or by volcanic lavas.

Unlike terrestrial craters, those on Venus are not eroded, because there is no surface water. There are also no small craters, because the smaller meteorites burn up in the thick atmosphere. Also the debris ejected by the impacts is fluidised by the atmospheric gas when it is compressed, and debris flows travel considerable distances from the impact sites, flowing downhill ([Figure 7](#)).



Figure 7: The crater Markham (diameter 69.5 km, -4.1°N, 155.6°E) in the Rusalka Planitia, with outflow deposits extending 370 km from the crater rim. Radar-bright outflows are a distinctive characteristic of many Venusian craters. The details of the genesis of these outflows are not clear. High atmospheric pressure and temperature favour the production of melted material at the instant of impact. One possible mode of the emplacement of outflows may involve a gliding motion of packets of melts over an entrapped atmospheric cushion. Since impactors with large kinetic energy produce larger amounts of melt, outflows tend to be more common among large craters. This observation is not a strict rule, however, since the relative occurrence of crater outflows seems to decline for the largest craters. Singular characteristics of crater outflows are their thinness and their length.

Impacts are important because they are at present the only way of dating the surface. Surprisingly the surface of Venus has an age of between 0.3 and 0.5 Ga, and shows no significant age variations with position on the planet. So the surface of Venus is quite unlike that of Earth: there are no systematic variations in lithospheric age as there are in the oceans, and almost no evidence for plate tectonics.

The SAR also made beautiful images of volcanoes and lava flows. Many of the flows on Venus are very large, and are often not clearly related to any tectonic features. Figure 8 shows a low viscosity flow, probably of basalt.

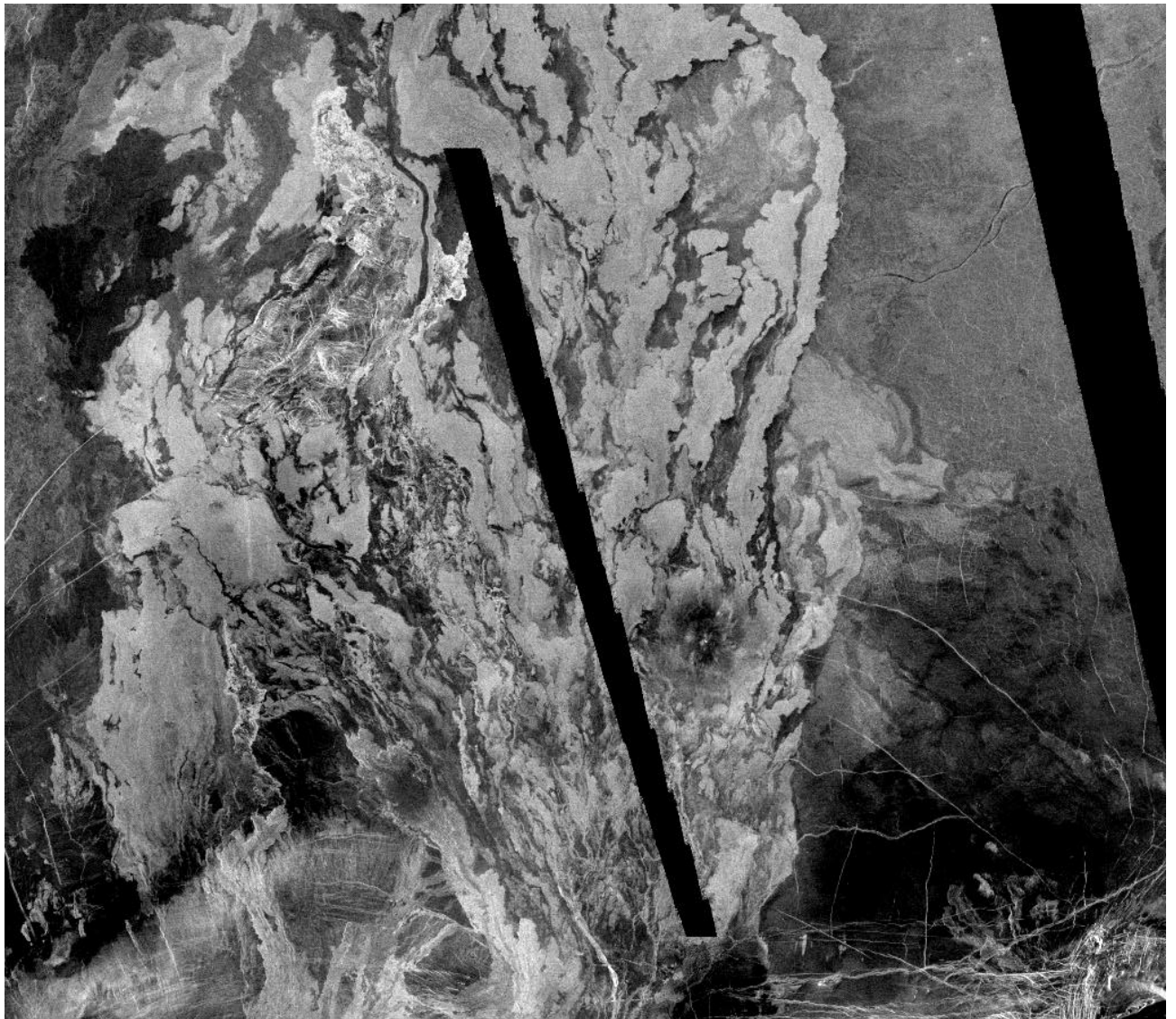


Figure 8: This image shows most of the Mylitta Fluctus lava flow field in southern Lavinia Planitia (55° S, 355° E). The flow field measures about 900 km in full length, and is about 450 km across. Individual flows measure tens of kilometres wide and hundreds of kilometres in length. The flows were erupted from a volcanic centre off the south (lower) part of the image and flowed northwards (up the image). The dark band in the centre of the image is a data gap. Differences in the brightness of the flows relate to their surface roughness, the brighter flows being rougher in surface texture.

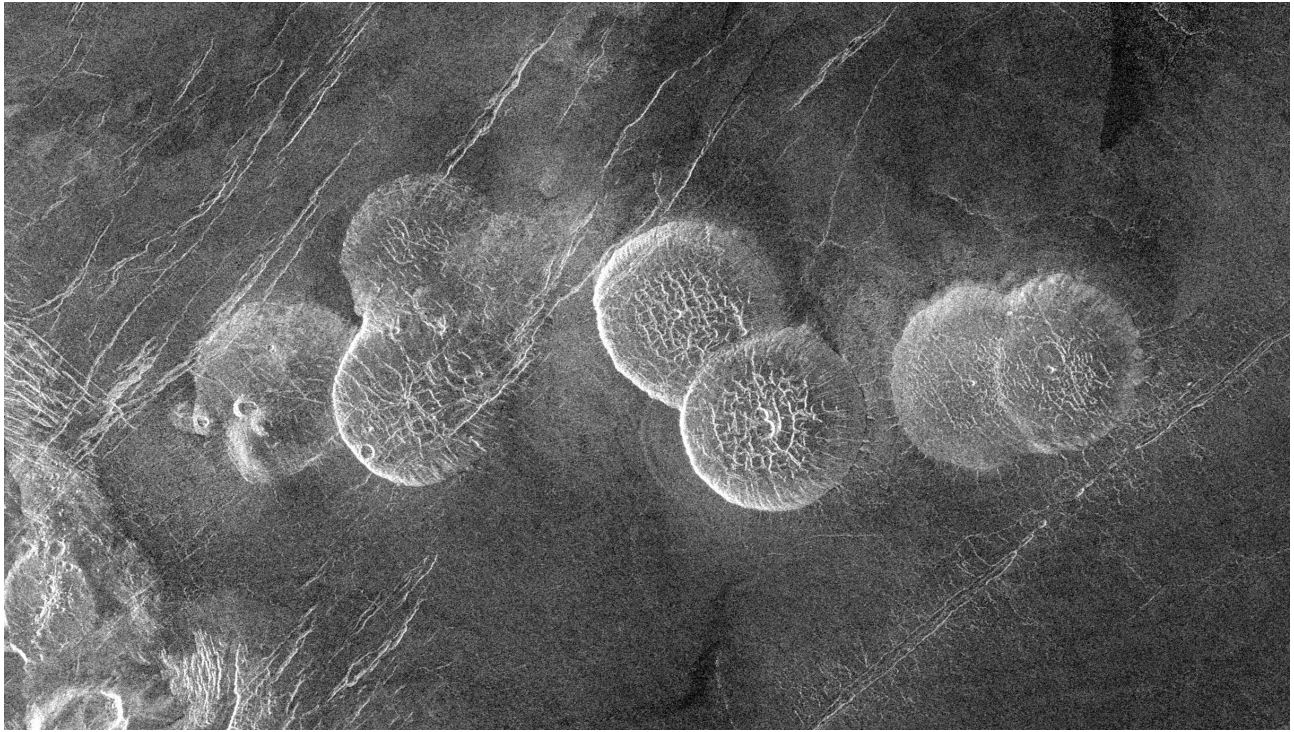


Figure 9: The eastern edge of Alpha Regio is shown in this image centered at 30° S, 11.8° E. Seven circular, dome-like hills, averaging 25 km in diameter with maximum heights of 750 m dominate the scene. These features are interpreted as very thick lava flows that came from an opening on the relatively level ground, which allowed the lava to flow in an even pattern outward from the opening. The complex fractures on top of the domes suggest that if the domes were created by lava flows, a cooled outer layer formed and then further lava flowing in the interior stretched the surface. The domes may be similar to volcanic domes on Earth. Some of the fractures on the plains cut through the domes, while others appear to be covered by the domes. This indicates that active processes pre-date and post-date the dome-like hills.

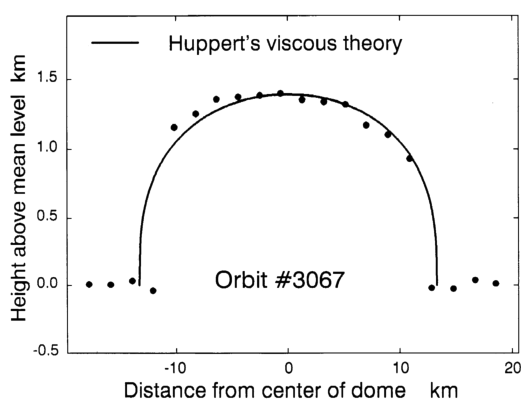
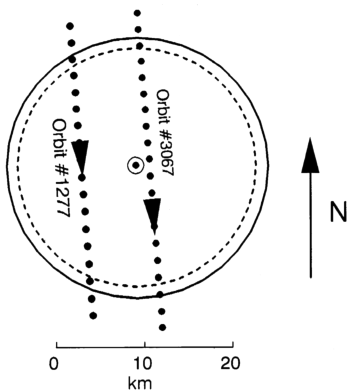


Figure 10: A fit to the pancake dome elevation using a model based on the spreading of a viscous drop. (McKenzie et al., 1992)

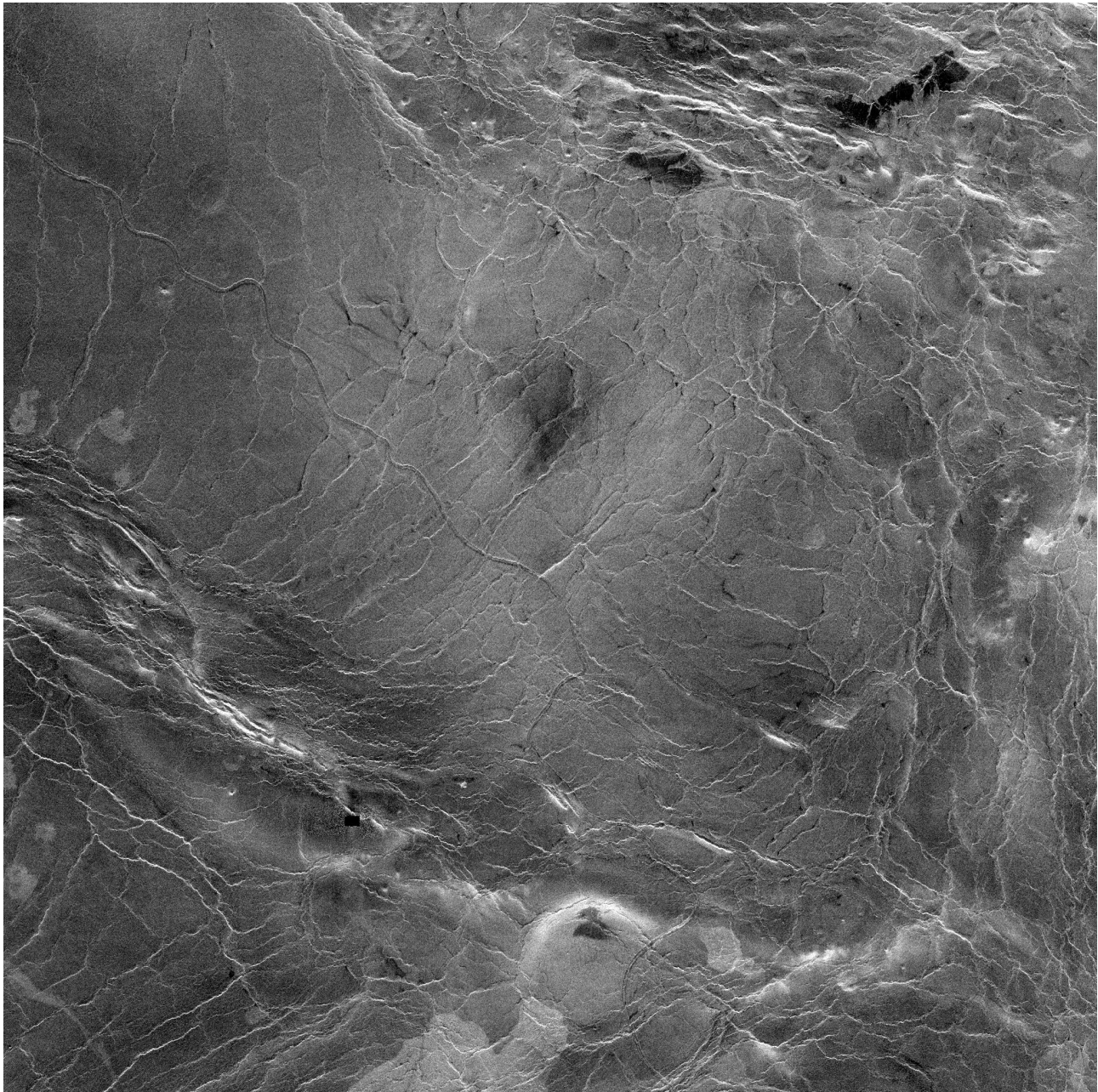


Figure 11: This image from 49° N, 165° E shows a 600 km segment of the longest channel discovered on Venus to date. The channel is approximately 1.8 km wide. At more than 7,000 km long, it is several hundred kilometres longer than the Nile River, Earth's longest river, thus making it the longest known channel in the solar system. Both ends of the channel are obscured, however, so its original length is unknown. The channel was initially discovered by the Soviet Venera 15-16 orbiters which, in spite of their 1 km resolution, detected more than 1,000 kilometres of the channel. These channel-like features are common on the plains of Venus. In some places they appear to have been formed by lava which may have melted or thermally eroded a path over the plains' surface. Most are 1 to 3 km wide. They resemble terrestrial meandering rivers in some aspects, with meanders, cutoff bows and abandoned channel segments. However, Venus channels are not as tightly sinuous as terrestrial rivers. Most are partly buried by younger lava plains, making their sources difficult to identify. In addition, they appear to run both upslope and downslope, suggesting that the plains were warped by regional tectonism after channel formation.

Magellan also imaged large circular features of internal origin, called coronae. We do not yet understand how these are formed. The one shown in [Figure 12](#) is the largest on Venus.

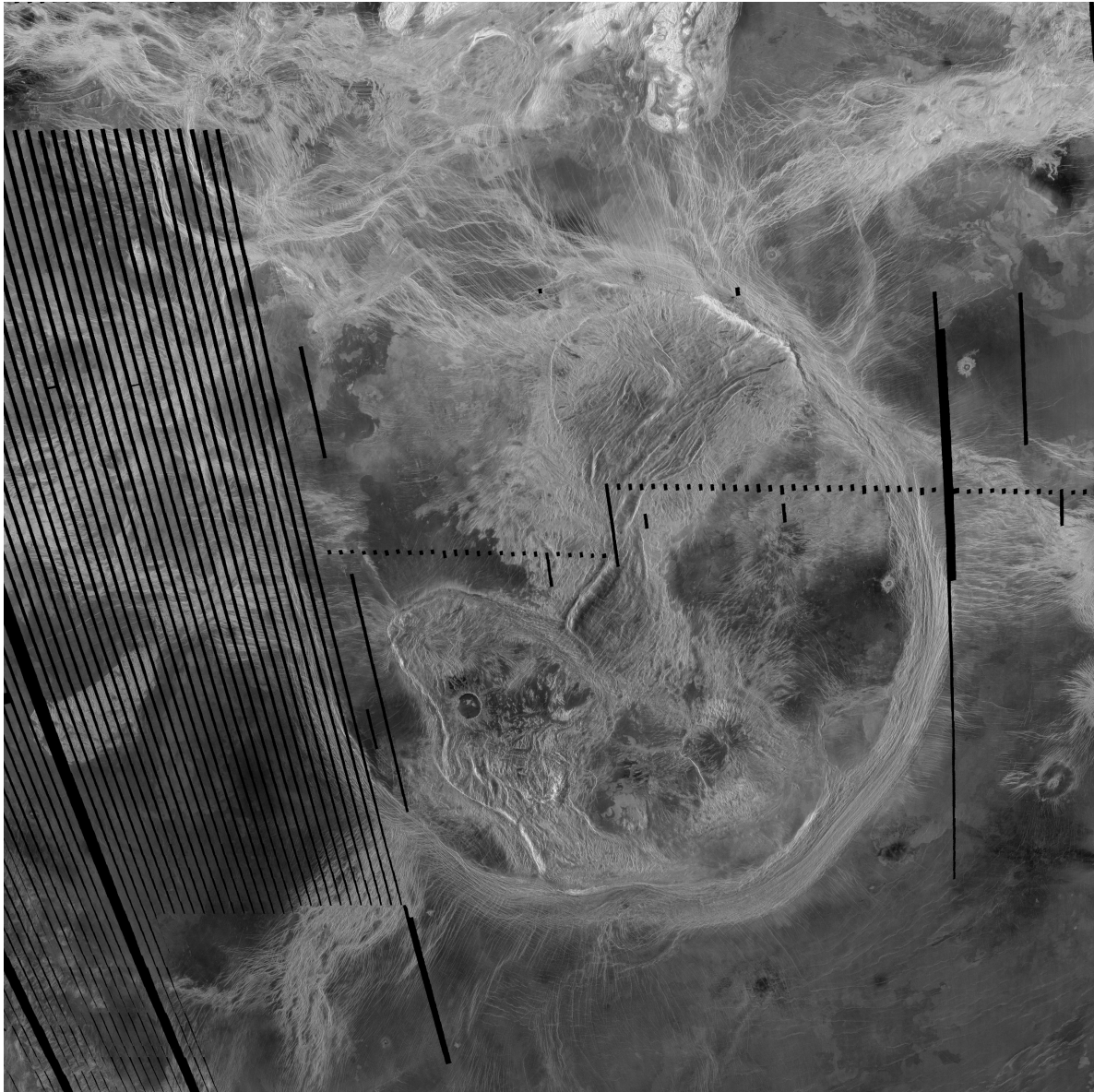


Figure 12: This spectacular Magellan image is centered on 30°S , 135°E , spans 3500 km from east to west (left to right), and shows the near-circular trough of Artemis Chasma. Its circular shape and size (2100 km in diameter) make Artemis the largest corona identified to date on the surface of Venus. Coronae are characterized by a ring of concentric features surrounding an interior which typically contains fractures of varying orientations and volcanic features ranging from individual flows and small (<20 km) volcanoes up to large (>100 km) shield volcanoes. Artemis contains complex systems of fractures, numerous flows and small volcanoes, and at least two impact craters, the larger of which is located in the lower left (southwest) quadrant of the feature. The ring of fractures that defines Artemis forms a steep trough with raised rims approximately 120 km wide and with as much as 2.5 km of relief from the rim crest to the bottom of the trough. Most coronae are thought to be related to upwelling of hot material from the interior of Venus in the form of plumes or diapirs, and Artemis may be an extensional trough related to such an upwelling event. Raised-rim troughs are most commonly found to be extensional features (those formed by forces which tend to pull apart the crust and lithosphere of a planet) but the unusual size and circularity of Artemis have led to the alternate suggestion that it may be a zone of intense compression and underthrusting, similar to oceanic subduction zones on Earth.

The last measurements that Magellan made before it was destroyed were of the gravity field. Figure 13 shows 5 milligal contours of the gravity g , and 200 m contours of the topography h , and residual topography $h - g/Z$, where $Z = 50$ milligals/km, the relationship from the convective models. So this last plot shows topography that is supported by crustal thickness variations, rather than by convection. The shortest wavelength shown in the figure is 600 km, and at this and longer wavelengths elastic support of the topography is not important. So the first plot, of g , shows the convective planform, which is very similar to that expected for high Rayleigh number convection. A striking feature of Venus is that several of the largest topographic features are convectively supported. This behaviour is unlike Earth, and requires a mantle viscosity that is a factor of ten or more greater than that of Earth. This difference is probably also the result of the absence of water.

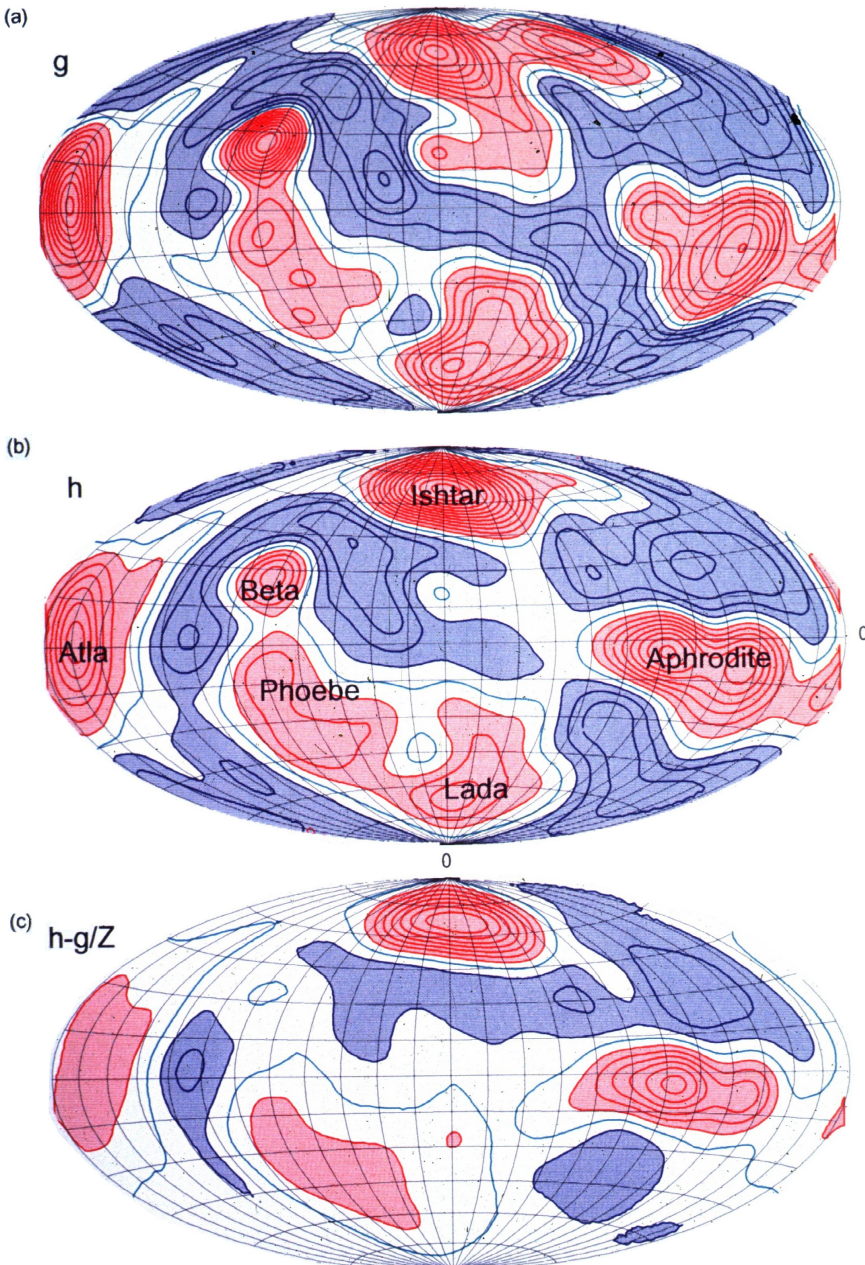


Figure 13: Low pass gravity (a), with a 5 mGal contour interval, topography (b), and residual topography (c) with a 200 m contour interval, for Venus with 0°N, 0°E at the center. (McKenzie, 1994)

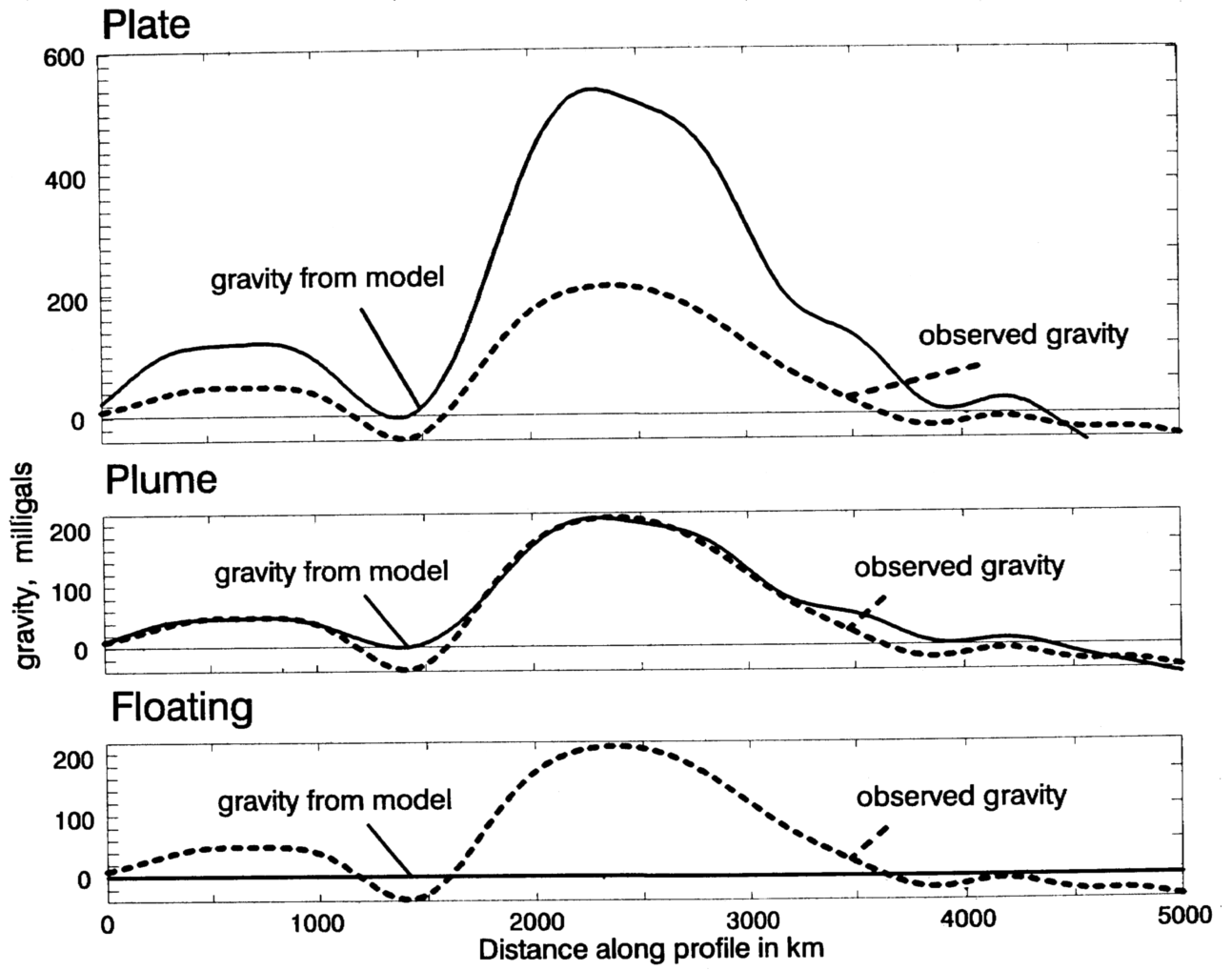


Figure 14: Observed gravity profile across Beta on Venus (dashed lines). Solid lines give model curves for gravity calculated from the topography assuming (a) uncompensated topography $Z \sim 140 \text{ mGal km}^{-1}$, (b) convectively supported topography $Z \sim 50 \text{ mGal km}^{-1}$, and (c) isostatically compensated topography $Z \sim 0 \text{ mGal km}^{-1}$. The gravity profile is best explained by convective support.

We can also estimate T_e in the same way as we did for the Earth, by Fourier transforming the topography and the gravity field, and then calculating Z the admittance.

The full expression for $Z(k)$ is

$$Z(k) = 2\pi(\rho_c - \rho_w)G \left[1 - \frac{\exp(-kt_c)}{1 + Dk^4/g(\rho_m - \rho_c)} \right]$$

where k is the wavenumber ($= 2\pi/\lambda$ where λ is the wavelength), $D = ET_e^3/12(1 - \sigma^2)$, E is Young's modulus and σ Poisson's ratio, ρ_w is the density of the fluid above the topography ($= 0$ for Venus, Mars and the continents, 1030 kg/m^3 for the oceans), t_c is the crustal thickness, g the acceleration due to gravity, and ρ_m the density of the mantle.

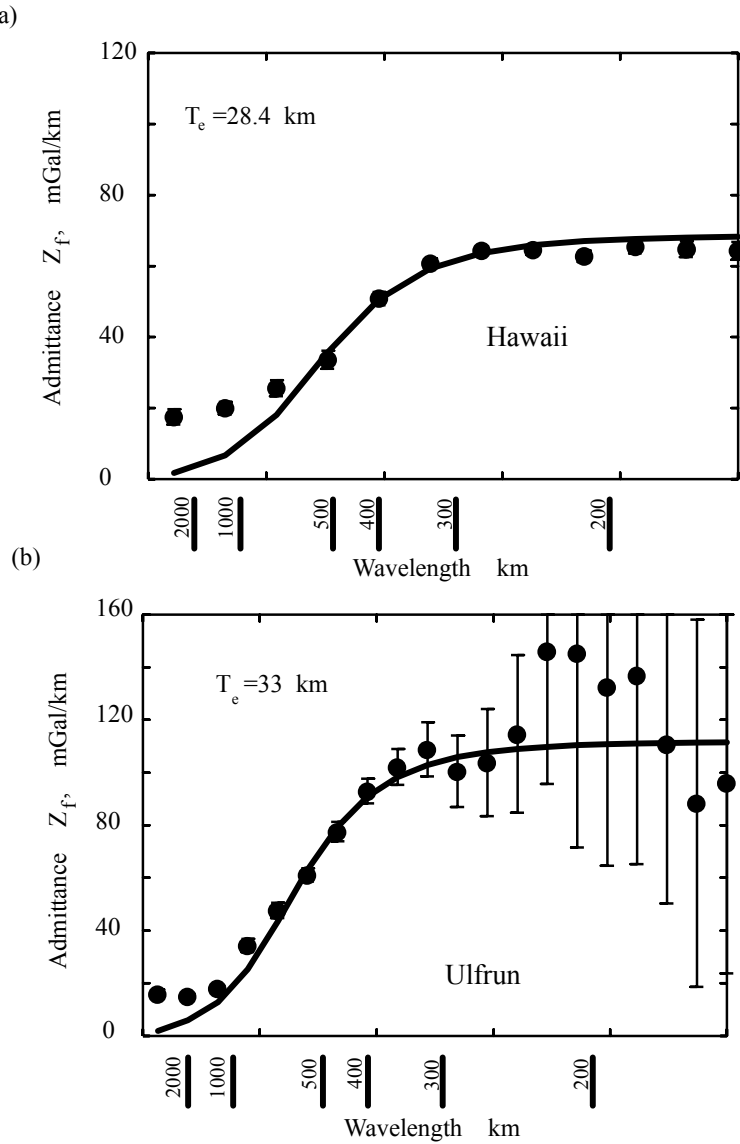


Figure 15: Admittance plots for (a) Hawaii on Earth and (b) the Ulfrun region of Venus (-20° to 40°N, -145° to -105°E). Dots are admittance values calculated from observed and calculated two-dimensional gridded line-of-sight acceleration. Vertical bars show one standard deviation. The solid curve is the theoretical admittance for a specified elastic thickness. (Nimmo and McKenzie, 1998)

As we have seen, there are substantial variations of T_e on Earth. Similar plots for Venus, of which one is shown from the Ulfrun region, can all be fitted with a value of T_e of about 30 km.

This value is larger than one would expect for the surface temperature of 430°C. We believe that the Venusian lithosphere can support elastic stresses at such high temperatures because it is dry, and that the variations of T_e are small because Venus is a one-plate planet with a mean age of the surface that is considerably greater than the thermal time constant of the lithosphere.

Figures 16 and 17 summarise what we have discovered about the interior of Venus from gravity and other observations. The thickness of the elastic part of the lithosphere comes from estimates of T_e . We believe that the reason why the temperature at the base of the elastic layer is higher than it is on Earth is because Venus is dry. The estimate of the lithospheric thickness is controlled by the solidus. There is clear evidence of melt generation on Venus, but the amount is constrained by the presence of old craters. If the lithosphere is too thin, these would be buried beneath lava flows. The structure of the plume in Figure 17 is controlled by the viscosity of the mantle, which needs to be about ten times that of the Earth's mantle to be able to support the convective topography above plumes. This difference is also likely to be the result of the mantle of Venus being so dry.

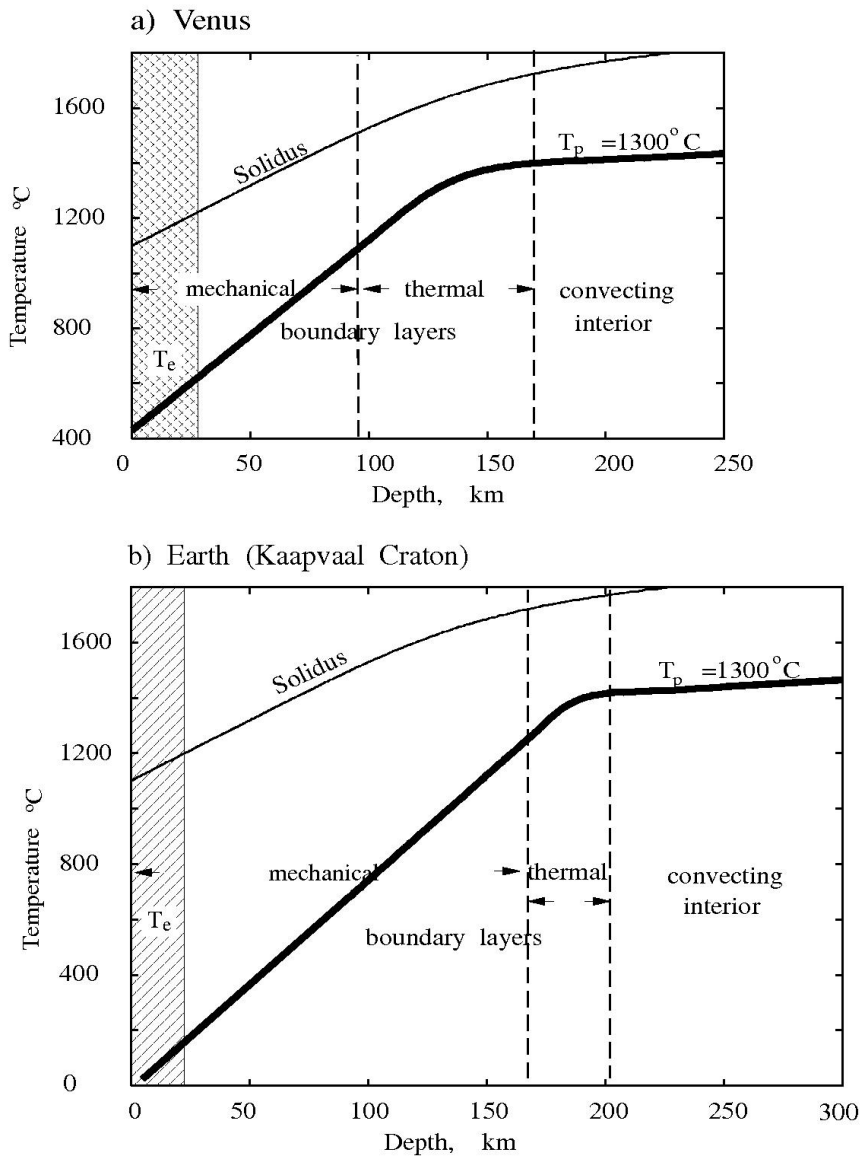


Figure 16: Comparison of the lithospheric structure of Venus with that of the Kaapvaal Craton of South Africa. Bold line is the geotherm; the thin line is the solidus; diagonal shaded region represents the maximum likely elastic thickness of the lithosphere. (Nimmo and McKenzie, 1998)

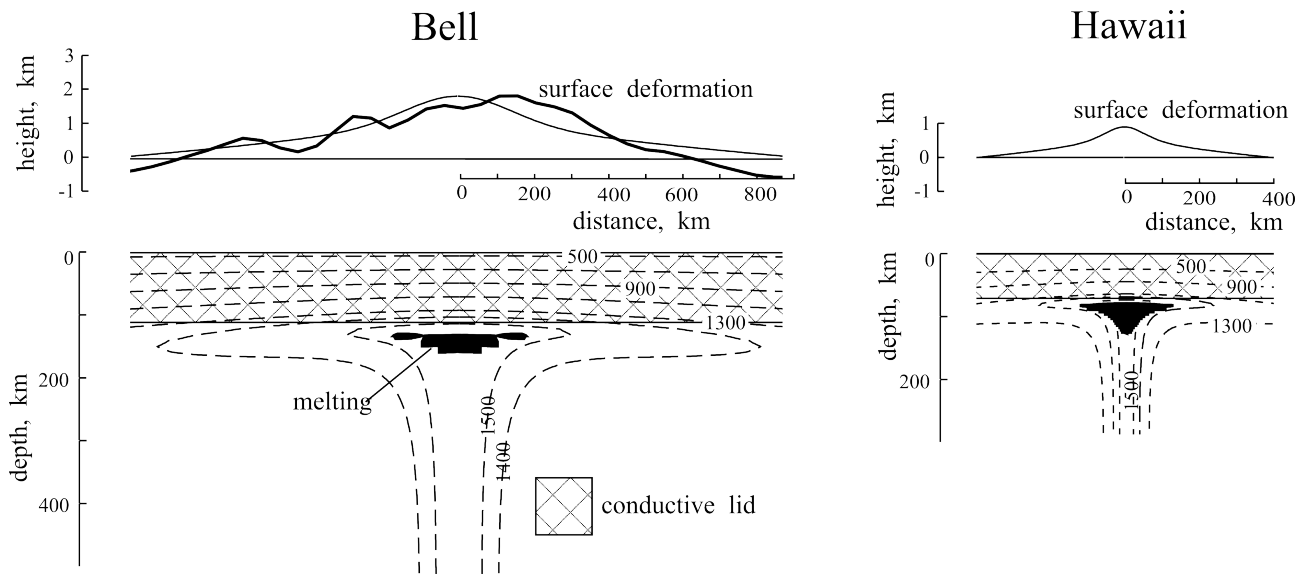


Figure 17: Summary diagrams showing the regions of melting and the surface deformation associated with the convection. Profiles across Bell on Venus (30°N , 47°E) and Hawaii on Earth. The diagonal shading indicates the mechanical boundary layer and melt generation occurs in the region in which the instantaneous melt production rate exceeds 0. Dashed lines are temperature contours in degrees Celsius; vertical exaggeration 1.7:1. (Nimmo and McKenzie, 1998)

Mars

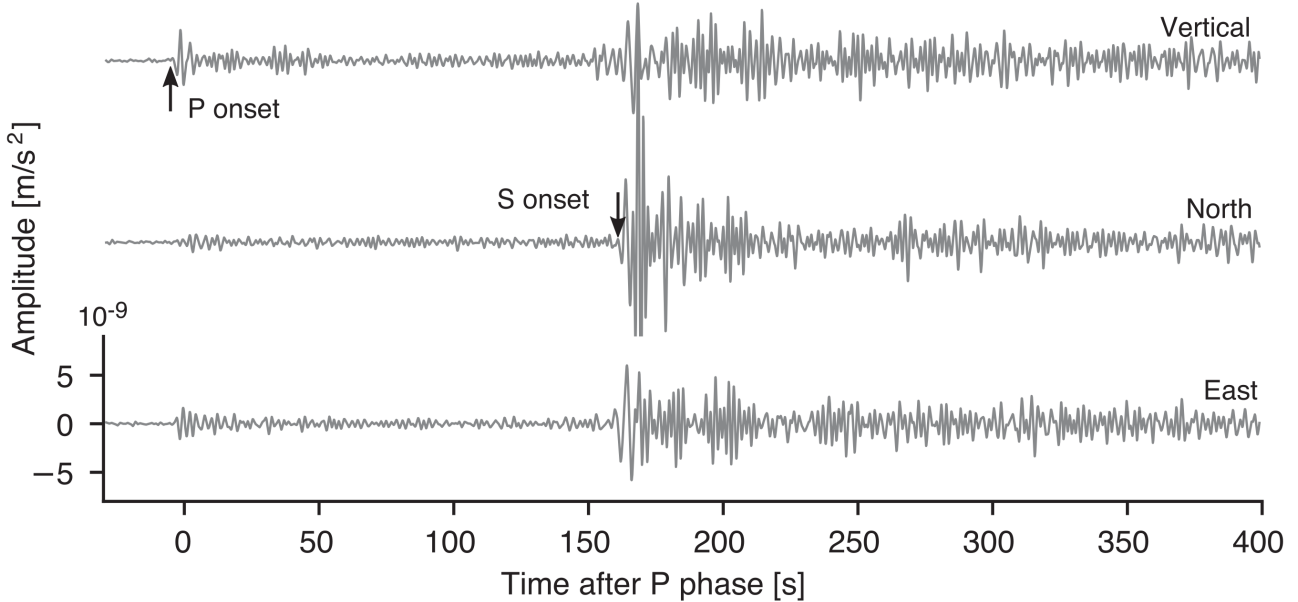


Figure 18: A marsquake recorded by the InSight seismometer. Three-component broadband-filtered (1.5 to 8 s) seismogram of event S0235b. The direct P- and S-wave arrivals can be clearly seen and are indicated by the vertical arrows. (Khan et al., 2021)

Mars has seen much more intensive study than Venus, with a wide variety of satellites in orbit and rovers on the surface. From a geophysics perspective, a great deal of excitement has been generated by NASA's InSight lander which touched down on Mars on 26th November 2018 (<http://insight.jpl.nasa.gov/>). The InSight lander has a number of geophysical instruments onboard, most importantly a seismometer, and made the first ever recordings of marsquakes. A seismogram from InSight is shown in Figure 18. So far over 1,300 marsquakes have been recorded, the largest of which is magnitude 5.

The main challenge with seismology on Mars is that there is only a single station. Many standard seismological techniques rely on data from multiple stations and simply can't be used with the InSight data. For example, on Earth earthquakes can be located fairly easily using the arrival times at multiple stations. Locating marsquakes is more subtle. One key piece of information that is used is the differential travel time between the direct P and direct S arrivals (Figure 18). If you know roughly what the P and S wave speeds are in the rocks you can use this differential travel time to work out the distance to the earthquake source. This gives you a location within a ring around the lander as illustrated in Figure 19. To fully locate the earthquake one needs to also estimate the back-azimuth, and this is harder, but can be done by estimating the polarization of the waves from the 3-component data. Most marsquakes have been located around 30° away from the lander in a graben system in Cerberus Fossae, but there have been some recent reports of events much further away in Valles Marineris (Figure 19).

One of the main goals of the InSight mission is to provide insights(!) into the structure of the deep interior of Mars. To do this requires using more of the seismogram than the direct arrivals, such as the later reflected arrivals PP and PPP whose differential travel times with P are sensitive to variations in velocity with depth (Figure 20). Velocity models that have been inferred from such data are shown in Figure 21a, and indicate a crust approximately 50 km thick, and a lithosphere around 400 to 500 km thick. Moreover, the phases ScS (S wave reflecting off the core) and Pdiff (P wave diffracting along the core-mantle boundary) have been identified (Figures 22 and 23) whose timing places constraints on the size of the Martian core. The InSight estimates of core size are at the large end of pre-mission estimates, at around

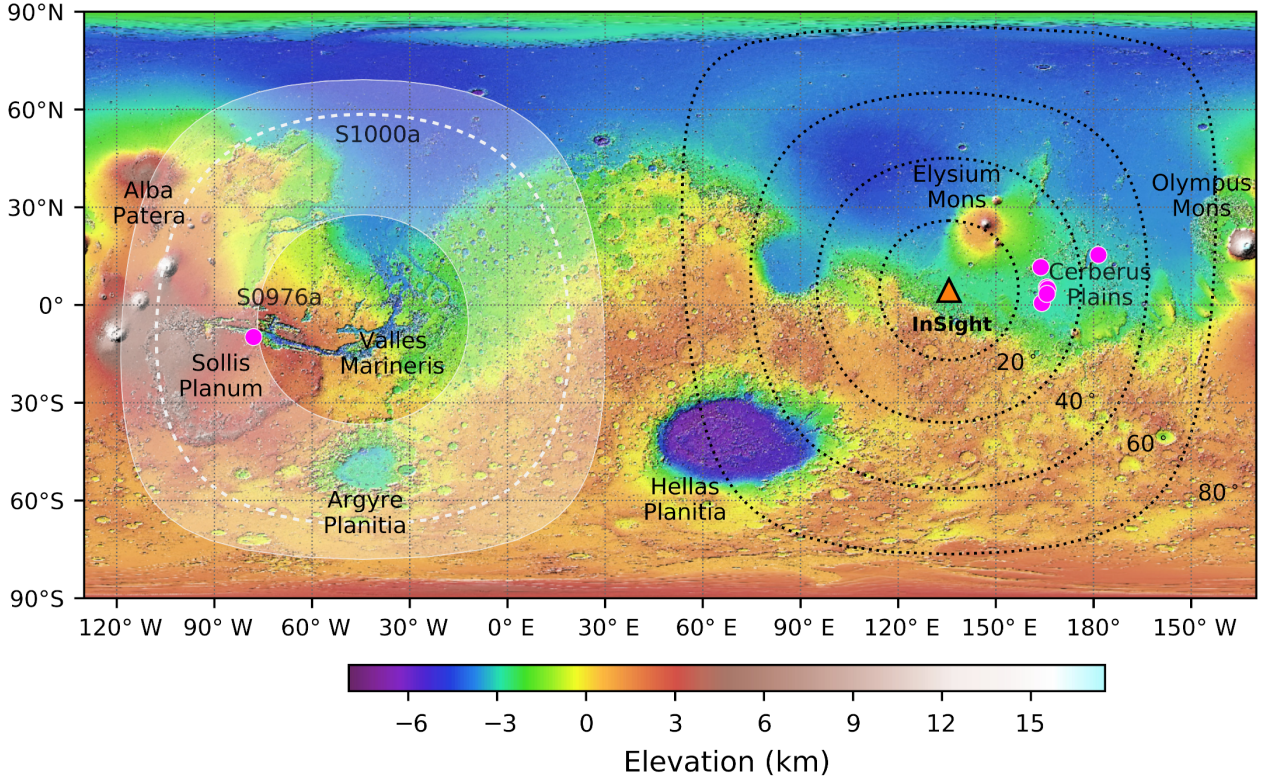


Figure 19: Mars seismicity location map. Mars surface relief map showing InSight's location (orange triangle), the location of other located marsquakes (magenta dots) that cluster around 30° distance, close to Cerberus Fossae, and S0976a, located within Valles Marineris just north of Sollis Planum. Because no back azimuth can be determined for S1000a, its location is predicted to be somewhere within the shaded region between 107° and 147° from InSight. The event's preferred distance (116°) is marked with the white dashed line. The black dotted lines mark radii around InSight up to 80° . The background image is from the Mars Orbiter Laser Altimeter. (Horleston et al., 2022)

1830 ± 40 km.

Remarkably, there have been meteoroid impacts detected by InSight that have been witnessed by orbital imaging (Figure 24). Comparison between the InSight-estimated locations and the true locations observed from space has provided a good validation of the marsquake location techniques being used. Moreover, the impacts have also been associated with the first ever detection of surface waves on Mars. No doubt many more insights lie ahead as the data is more carefully analysed!

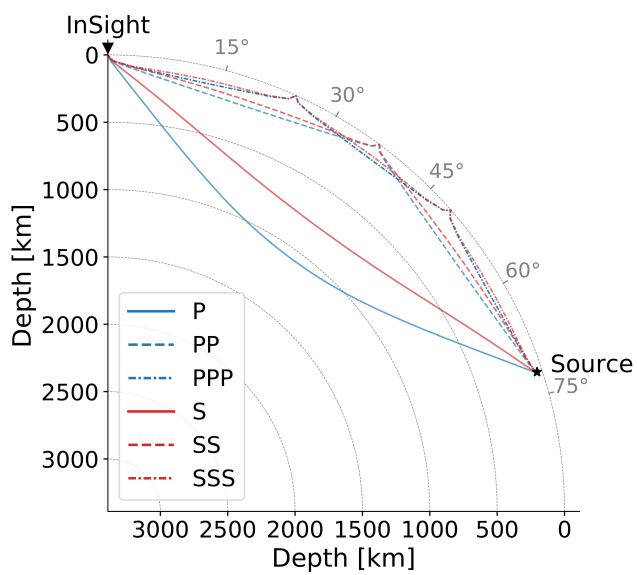


Figure 20: Ray paths for the seismic body wave phases (direct P- and S-wave and surface reflections PP, PPP, SS, and SSS) on Mars with a source located at 50 km depth. (Khan et al., 2021)

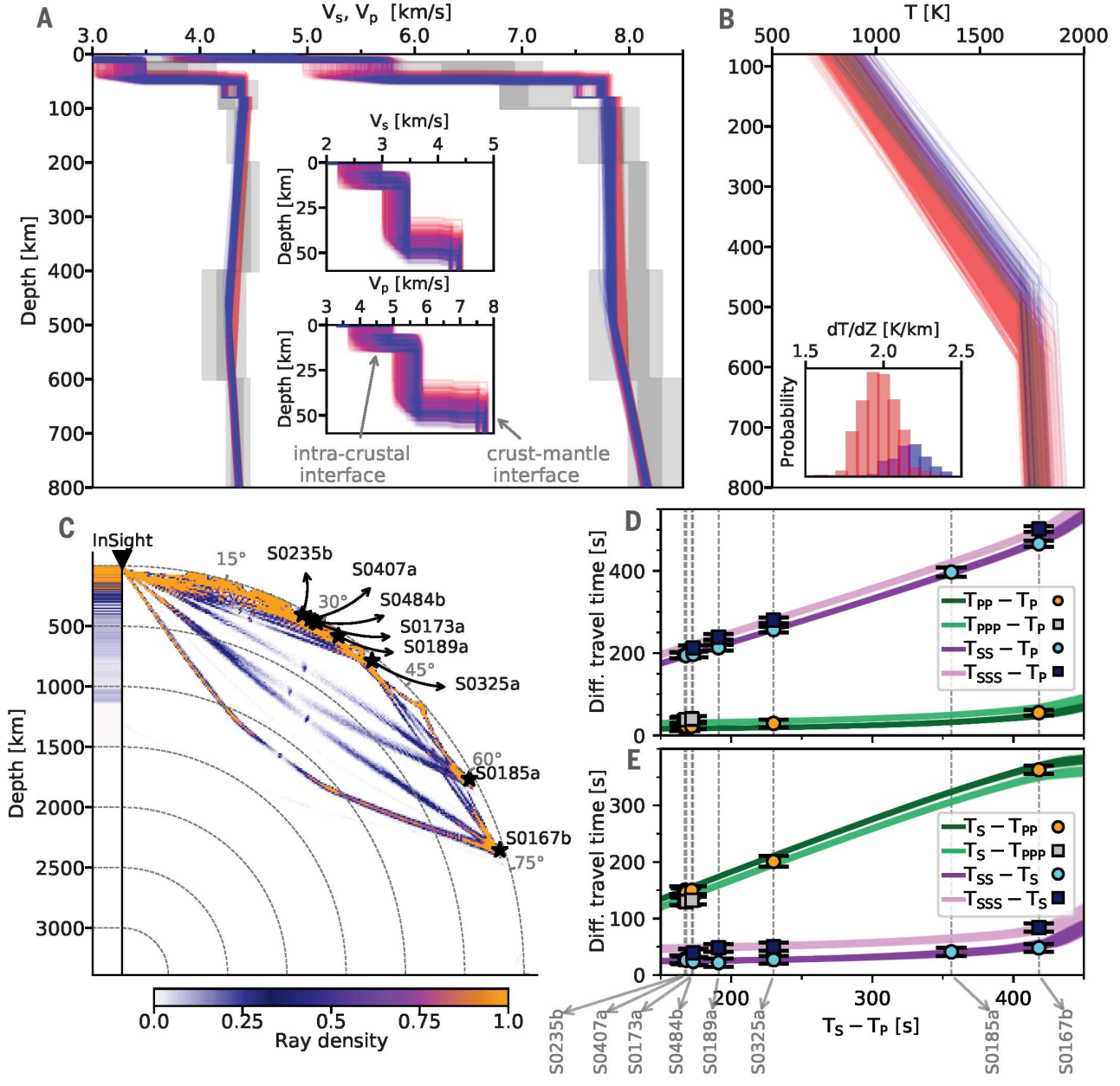


Figure 21: Summary of Mars' upper mantle structure. (A and B) Inverted S- and P-wave velocity and geothermal profiles. Colored (red and blue) and gray-shaded models are obtained from geophysical and seismic inversions, respectively. Insets show the distribution of sampled crustal S- and P-wave velocity structure and lithospheric geothermal gradients (dT/dz), respectively. Profiles are color-coded according to lithospheric thickness: 400 to 500 km (blue) and 500 to 600 km (red). The lithospheric thermal gradient is determined from the temperature at the crust-mantle interface and at the bottom of the lithosphere and from the difference in depth between the two points. Gray-shaded contours in (A) indicate the 50%, 75%, and 90% credible intervals computed from the distribution of models inverted using a purely seismic parametrization. (C) Body-wave ray path geometry for the eight events (labeled S0167b, S0185a, etc.) Color bar denotes ray path density (i.e., number of rays passing through a given area) based on inverted models shown in (A), which explains the diffuseness of ray paths and source locations. The column to the left of “InSight” shows radial sensitivity, computed as the integrated ray path density with epicentral distance. (D and E) Differential body-wave travel-time misfits for all sampled models shown in (A). Green and purple lines denote differential travel times computed using the inverted models; squares and circles indicate the observations including error bars. (Khan et al., 2021)

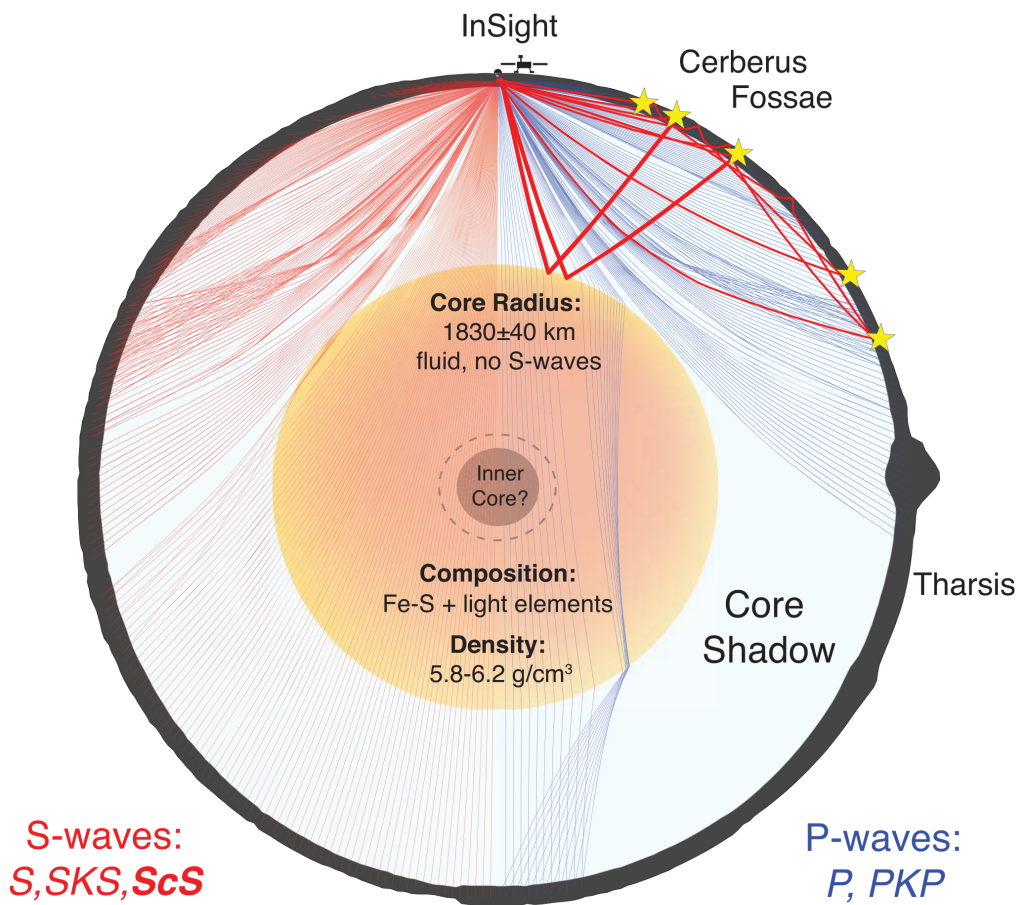


Figure 22: Schematic diagram of Mars' interior structure. The cross section depicts the core-induced shadow zone for seismic waves. The surface topography is a cut through the Mars Orbiter Laser Altimeter map on a great circle arc from InSight through Olympus Mons. The S-wave shadow zone is minimal and probably filled by diffracted S waves (Sdiff), whereas the P-wave shadow zone is large and contains specifically the Tharsis region. The existence of an inner core cannot be determined by current data, and the seismic ray paths shown assume no inner core. Topography and InSight lander are exaggerated in scale. (Stähler et al., 2021)

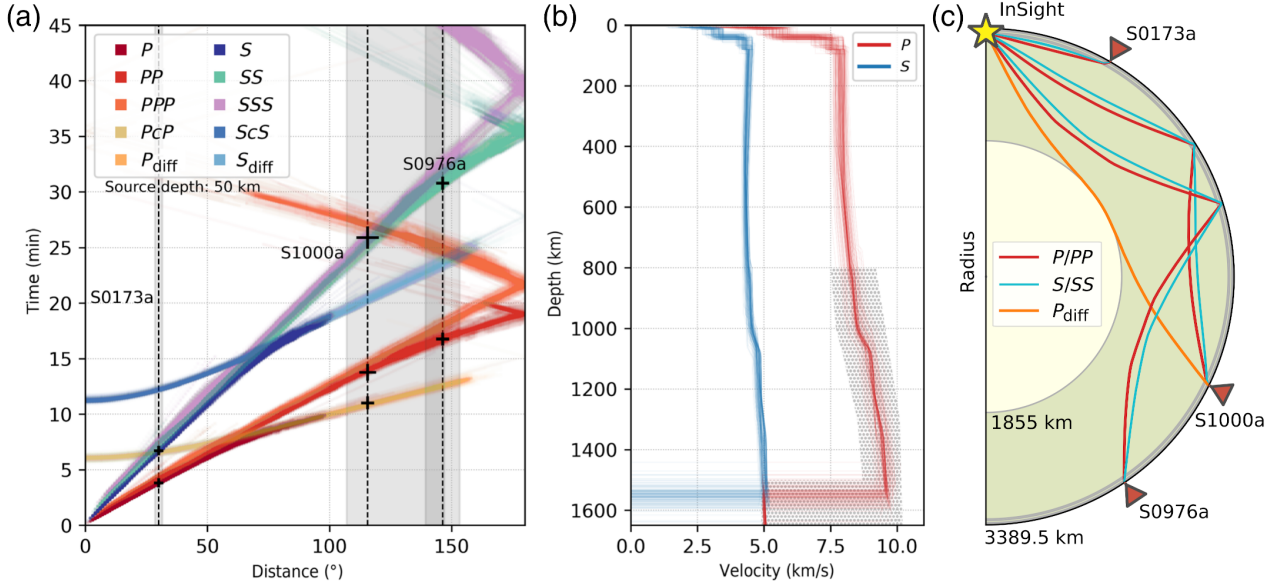


Figure 23: Summary of Martian interior models from Stähler et al. (2021) and ray paths for seismic phases for three events. (a) The travel time curves are computed for a source depth of 50 km. The phase picks that the Marsquake Service (MQS) identified for these events are indicated with crosses, with varying symbol sizes to schematically reflect the pick uncertainties. The distant events are S1000a and S0976a. For comparison, also shown is S0173a, an event at 30° that locates at Cerberus Fossae. For all three events, high-amplitude phase arrivals have been identified as direct P/S for S0173a and single free-surface reflections PP/SS for S1000a and S0976a. For S1000a, a weak Pdiff phase that is diffracted along the core–mantle boundary is also identified. The vertical dashed lines and gray shaded bars mark the event distances and uncertainties. (b) The structural models are not constrained by observations for depths below ~ 800 km for P waves (hatched region; Khan et al. (2021)), hence the Pdiff travel times are purely from model predictions. (c) Illustrates the ray paths of the identified phases using a Mars model with a core radius of 1855 km. (Horleston et al., 2022)

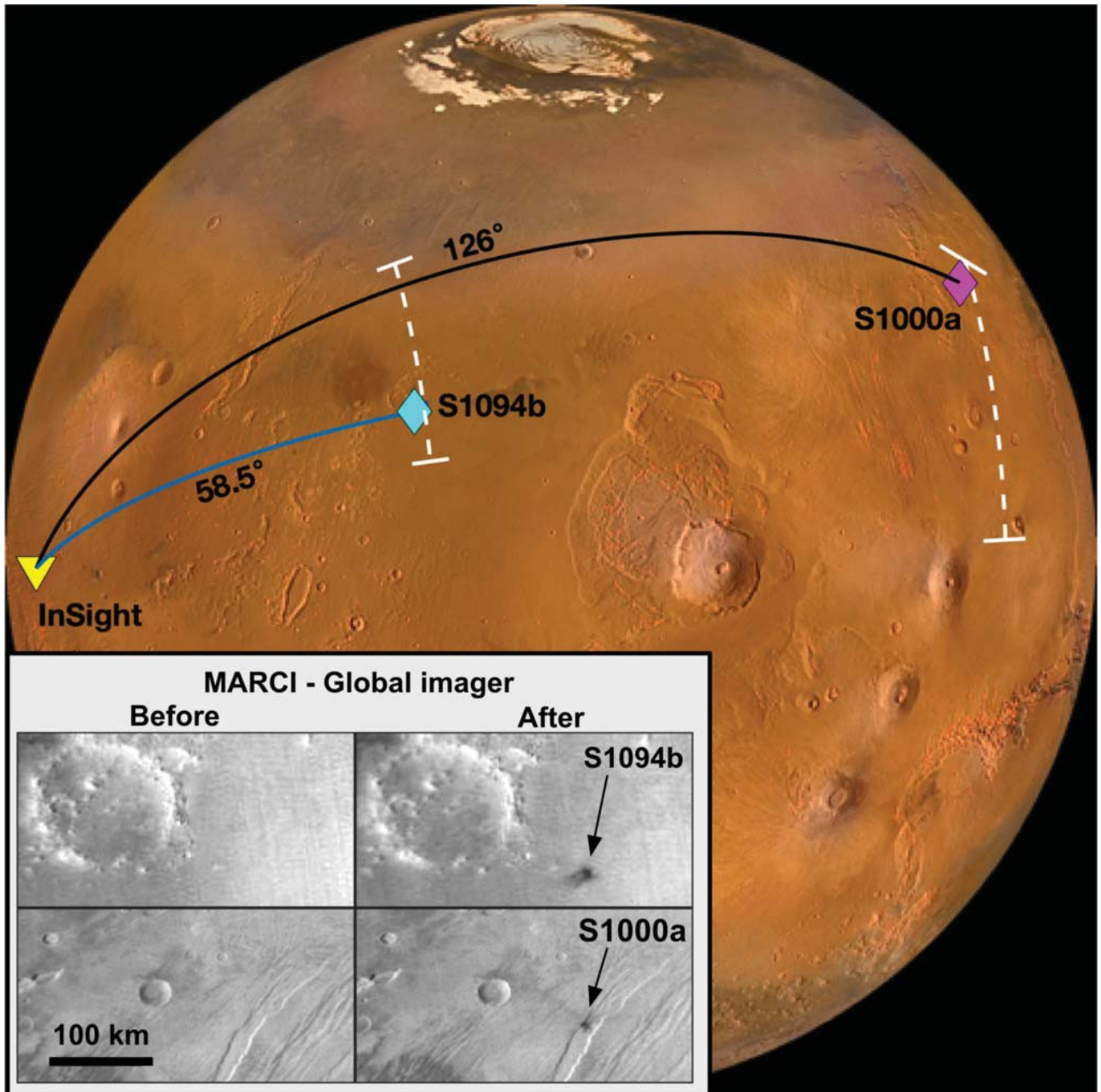


Figure 24: Impact event location map from Posiolova et al. (2022). The location of the impact craters (diamonds) and the InSight lander (yellow triangle) are shown. The S1094b crater is located at 34.80°N , 189.92°E in Amazonis Planitia. The S1000a crater is located at 38.11°N , 280.12°E in Tempe Terra. The great-circle paths between the new craters and InSight are superimposed onto the underlying globe image derived from MARCI, Mars Orbiter Camer, and Mars Orbiter Laser Altimeter (MOLA) data. The seismic epicentral distance estimates are indicated by the dashed white lines that extend over the azimuthal uncertainty estimate. The inset shows MARCI images from before and after the impacts.

References

- Horleston A.C., et al., 2022. The Far Side of Mars: Two Distant Marsquakes Detected by InSight. *The Seismic Record* 2, 88–99. doi:[10.1785/0320220007](https://doi.org/10.1785/0320220007).
- Khan A., et al., 2021. Upper mantle structure of Mars from InSight seismic data. *Science* 373, 434–438. doi:[10.1126/science.abf2966](https://doi.org/10.1126/science.abf2966).
- McKenzie D., 1994. The Relationship between Topography and Gravity on Earth and Venus. *Icarus* 112, 55–88. doi:[10.1006/icar.1994.1170](https://doi.org/10.1006/icar.1994.1170).
- McKenzie D., Ford P.G., Liu F., and Pettengill G.H., 1992. Pancakelike Domes on Venus. *J. Geophys. Res.-Planets* 97, 15967–15976. doi:[10.1029/92JE01349](https://doi.org/10.1029/92JE01349).
- Nimmo F. and McKenzie D., 1998. Volcanism and Tectonics on Venus. *Annual Review of Earth and Planetary Sciences* 26, 23–51. doi:[10.1146/annurev.earth.26.1.23](https://doi.org/10.1146/annurev.earth.26.1.23).
- Posiolova L.V., et al., 2022. Largest recent impact craters on Mars: Orbital imaging and surface seismic co-investigation. *Science* 378, 412–417. doi:[10.1126/science.abq7704](https://doi.org/10.1126/science.abq7704).
- Stähler S.C., et al., 2021. Seismic detection of the martian core. *Science* 373, 443–448. doi:[10.1126/science.abi7730](https://doi.org/10.1126/science.abi7730).

You are not expected to read any of these references. All the Magellan SAR images can be viewed on Google Earth by downloading a data file from <http://topex.ucsd.edu/venus/index.html>